PACS numbers: 75.70.-i, 78.20.Bh, 78.20.Ls, 78.66.-w, 78.67.-n, 79.20.Rf

Optical and Magnetooptical Spectroscopy of the Nanostructural Multilayered Films: Possible Applications

Yu. V. Kudryavtsev, V. N. Uvarov, R. Gontarz[*], J. Dubowik[*],
Y. P. Lee[**], J. Y. Rhee[***], Yu. N. Makogon[****], and E. P. Pavlova[****]

*G. V. Kurdyumov Institute for Metal Physics, N. A. S. of the Ukraine,
36 Academician Vernadsky Blvd.,
UA-03680 Kyyiv-142, STM, Ukraine*
[*]*Institute of Molecular Physics, Polish Academy of Sciences,
60-179 Poznań, Poland*
[**]*q-Psi and Department of Physics, Hanyang University,
Seoul, 133-791 Korea*
[***]*Department of Physics, Hoseo University,
Asan, Choongnam, 336-795 Korea*
[****]*National Technical University of Ukraine 'Kyyiv Polytechnic Institute',
37 Pobedy Ave.,
Kyyiv, Ukraine*

В данной работе показаны возможности спектральной эллипсометрии и магнитооптической (МО) спектроскопии для изучения структуры и особенностей физических свойств многослойных металлических пленок (МСП) с толщинами составляющих слоев порядка единиц нанометров. Основной подход исследования базируется на сравнении экспериментально измеренных оптических и МО свойств МСП с модельными, полученными для различных моделей структуры МСП. Было показано, что данный подход позволяет выяснить природу необычных МО свойств, а также структуру интерфейсной области в МСП, состоящих из слоев благородных и $3d$-переходных металлов (ПМ). Также в работе продемонстрирована высокая чувствительность спектральной эллипсометрии для изучения твердотельных реакций в МСП $3d$-ПМ/Si, вызванных ионной бомбардировкой или термическим отжигом. Оптические свойства различных силицидов $3d$-ПМ, сформированных спонтанно либо в результате различных воздействий на МСП, были изучены экспериментально и сравнены с результатами теоретических первопринципных расчетов.

В даній роботі показано можливості спектральної еліпсометрії та магнетооптичної (МО) спектроскопії для вивчення структури та особливо-

стей фізичних властивостей багатошарових металевих плівок (БШП) з товщинами складаючих їх шарів порядку одиниць нанометрів. Основний підхід дослідження базується на порівнянні експериментально одержаних оптичних та МО властивостей БШП з модельними, які були одержані для різних моделів структури БШП. Було показано, що даний підхід дозволяє визначити природу незвичайних МО властивостей, а також природу інтерфейсної області БШП, які складаються з шарів благородних та $3d$-перехідних металів (ПМ). В роботі також показано високу чутливість спектральної еліпсометрії для вивчення твердотільних реакцій у БШП $3d$-ПМ/Si, зумовлених йонним бомбардуванням або термічним відпалом. Оптичні властивості різних силіцидів $3d$-ПМ, які сформувались спонтанно або завдяки зовнішньому впливу, було вивчено експериментально та порівняно з результатами теоретичних першопринципних розрахунків.

The aim of the paper is to show the potential of the spectroscopic ellipsometry and magnetooptical (MO) spectroscopy for probing of the multilayered films (MLF) with sublayer thickness of about a few nanometres. The main approach applied by us is based on the comparison of the experimental optical and MO properties with the simulated ones based on various models of the MLF. Specifically, as shown, such an approach can be useful for studying the nature of unusual MO properties and the interfaces in MLF comprising the noble and $3d$-transition metals ($3d$-TM). The high sensitivity of the applied spectroscopic methods for the monitoring of the solid-state reactions in the $3d$-TM/Si MLF induced by ion-beam treatment or by thermal annealing is also demonstrated. The optical properties of various silicides formed spontaneously or induced by various treatments at interfaces are evaluated experimentally and compared with the results of first-principle calculations.

INTRODUCTION

Recent discovery of new interesting physical phenomena (such as oscillating interlayer exchange coupling, giant magnetoresistance, unusual magnetooptical (MO) responses, quantum size effects) in the magnetic artificial structures like multilayered films (MLF) composed of alternated layers of ferromagnetic and nonmagnetic metals has prompted intensive research in this field.

Among the metallic multilayers, a specific place occupy the MLF composed of ferromagnetic $3d$-transition metals (TM) (mainly Co and Fe) and heavy noble metals (NM) because of the noticeable enhancement of the MO response in the near ultraviolet (UV) region

and significant potentials for their practical application as a storage media. The MO properties of the Co/Pt [1–6] and Fe/Au [7–13] MLF have been widely investigated experimentally and theoretically. The experimentally observed unusual MO response is attributed to the direct orbital hybridization between Pt(Au) and Co(Fe) atoms: the spin magnetization of the magnetic Fe(Co) atoms is transferred to the nonmagnetic Pt(Au) atoms and the stronger spin-orbit coupling of the heavy Pt(Au) atoms is transmitted to the Fe(Co) atoms [14]. However, in spite of a huge number of publications and of some attempts to determine the MO properties of the 'magnetic' Pt, for example, undertaken by Sato and co-workers by analyzing the MO spectra of Fe_xPt_{1-x} alloys [15], the MO properties of the 'pure' spin-polarized Pt and Au sublayers have not been yet confirmed.

For the correct interpretation of the experimental MO data, the actual MLF structure should be known. An undertaken theoretical attempt to interpret the experimental MO data for the Co/Pt MLF had no success without taking into account the interfacial regions [13]. Some quantitative agreement between the experimental and modelled Kerr rotation spectra was achieved by Weller and coworkers [1] for the Co/Pd MLF by solving the equations of the electromagnetic wave theory for the model, which considers also interfacial region between pure components. Nevertheless, the similar approach for the Co/Pt MLF failed partly owing to the irrelevant input data. The origin for the discrepancy between experimental and simulated data may originate from an inadequate model for the crystalline structure, and improper use of the optical and MO constants for the constituent sublayers, different from the real ones.

It is also well known that the MO response of the media is determined by their off-diagonal components of the dielectric function (DF) (related to the MO properties) as well as by their diagonal components of the DF (determining the optical properties). However, unlike MO properties, the optical properties of the Co/Pt and Fe/Au MLF are noticeably less investigated—only several publications related to Co/Pt and Fe/Au MLF can be mentioned [5, 13, 15]. At the same time, another possible explanation of such unusual MO properties of the Fe/Au layered structures was also suggested by Suzuki *et al.*: a new MO absorption appears due to formation of quantum well states in very thin Fe sublayers [16]. If so, the formation of these quantum well states should also found their manifestation in the optical properties of the Fe/Au MLF (while the first one, probably, not).

3d-transition metal (TM) silicides have been receiving a great attention in very-large-scale-integrated devices for interconnectors, gates, and source contacts due to low resistivity, good thermal stability and small mismatch with Si substrate. Therefore, the ability

to grow silicides on semiconductor materials in a more controlled manner has become a subject of increasingly importance. $3d$-TM silicide films are commonly fabricated by evaporation or sputtering of the single $3d$-TM layer onto Si substrate with a subsequent post-annealing. From a thermodynamical point of view, such a $3d$-TM silicide formation is a consequence of decrease in the free energy of the system through the solid-state reactions, until the thermally-stable end product is reached.

Apparently 'new' phenomena, in comparison with aforementioned case can be observed in the $3d$-TM/Si MLF structures: another consecution of phase appearance, the formation of metastable phases which are not identified in the equilibrium phase diagram [17], an extremely rapid growth (an 'explosive' reaction) [18], the formation of amorphous interlayers by a reaction between the crystalline sublayers [19]. Solid-state reactions between a $3d$-TM metal (for example, Ni, Co, and Fe) and a Si substrate and $3d$-TM/Si MLF during annealing have been studied intensively [18, 20−27]. It was found that the sequence of phase formation as well as the temperatures of their appearance depend on many factors, such as beginning layered structure, sublayer thicknesses, overall stoichiometry *etc*.

The employment of ion-beam mixing (IBM) creates additional perspectives for the silicide formation: it can lead to the interaction between neighbouring layers by the energetic incident ions under highly nonequilibrium conditions that the silicide formation can not be achievable by the conventional equilibrium techniques. This comprises not only the energy to activate the interfacial interaction but also the diffusion necessary to maintain the silicide growth. It was reported that a rich variety of the structures induced by ion-beam irradiation might be formed in $3d$-TM films deposited onto Si substrate [28−34].

Since the discovery of a strong antiferromagnetic (AF) interlayer coupling in Fe/Si MLF, the reactive formation of interfaces between Fe sublayers and the resultant interfacial structure appear to be problems of intriguing complexity and a subject of comprehensive study [35−43]. However, in spite of employment of many various experimental tools for study of the stoichiometry and structure of the interfacial regions in Fe/Si MLF (like soft-x-ray fluorescence and near-edge x-ray-absorption fine-structure spectroscopy [42], x-ray diffraction (XRD) [36], low-energy electron diffraction and Auger electron spectroscopy [41, 43], and direct cross-sectional transmission electron microscopy observations [37]), the nature of the spontaneously formed spacer in Fe/Si MLF is still open.

The ability to predict a phase formation sequence and phase decomposition during reactive deposition, solid-state reaction and ion-beam mixing in terms of the effective-heat-of-formation model

was illustrated by Pretorius *et al.* [44]. Nevertheless, in practice, in order to answer the question '*What product of the solid state reaction appears in the interfacial region of layered structures*?' an experimental tools sensitive to the local environment like nuclear magnetic resonance (NMR) or Mössbauer spectroscopies, in addition to the standard structural-analysis methods such as XRD or transmission-electron microscopy (TEM), should be employed. However, some of these local methods may have some constraints (for example, an existence of the nuclear magnetic moment for NMR) and cannot be employed for the all systems.

It is well known that both optical and MO properties of metals depend strongly on their electron energy structures which are correlated with the atomic and magnetic order. The spontaneous, thermally or IBM induced interdiffusion between $3d$-TM and Si layers in the $3d$-TM/Si MLF should change the chemical and atomic order in the reactive zone and also decrease the thickness of $3d$-TM sublayers (and hence the MO response from the layered system). The skin-penetration depth for most of the metals in the visible range of spectra is about 20–30 nm. This means that, for the MLF whose individual sublayer thickness is about of nanometres, the optical response carries out the information on tens of sublayers.

Evidently, the real structures and magnetic properties of the as-deposited and/or reacted MLF may be verified by a comparison between the experimental and computer-simulated optical and MO data, based on an appropriate model of the layered structure and the properties of the constituent sublayers.

Thus, it seems attractive to show the potential of noncontact and non-destructive spectroscopic ellipsometry (SE) and MO spectroscopy for *in situ* study of the peculiarities of the MO properties of $3d$-TM/NM MLF, spontaneous, thermally or IBM induced solid-state reactions in the $3d$-TM/Si MLF as well as for the investigation of the stoichiometry and properties of the interfacial regions which provide the AF coupling in Fe/Si MLF.

EXPERIMENTAL AND SIMULATION DETAILS

A. Experimental Procedure

The $3d$-TM/NM and $3d$-TM/Si MLF of different nominal overall stoichiometry, individual sublayer thicknesses and number of bilayer repetitions were prepared onto glass and single-crystalline Si-wafer substrates kept at room temperature (RT) by the computer-controlled double-pair target face-to-face sputtering technique. The basic pressure was about 1×10^{-6} Torr, an Ar pressure during the film deposition did not exceed 5×10^{-4} Torr, deposition rate was about 0.1 nm/s.

TABLE 1. The parameters of the investigated $3d$-TM/NM MLF.

Sample No.	Nominal MLF formula	Numbers of bilayers	Top layer	Buffer layer (nm)	Substrate	Nominal overall MLF composition
1	3.8 nm Co/1.34 nm Pt	50	Pt		glass	$Co_{0.24}Pt_{0.76}$
2	4.6 nm Co/1.36 nm Pt	50	Pt		glass	$Co_{0.27}Pt_{0.73}$
3	0.7 nm Co/1.25 nm Pt	44	Pt		glass	$Co_{0.38}Pt_{0.62}$
4	0.9 nm Co/1.44 nm Pt	40	Pt		glass	$Co_{0.41}Pt_{0.59}$
5	1.9 nm Co/1.43 nm Pt	33	Pt		glass	$Co_{0.59}Pt_{0.41}$
6	3.0 nm Fe/1.0 nm Au	20	Au	Au, 20	glass	$Fe_{0.81}Au_{0.19}$
7	3.0 nm Fe/2.0 nm Au	20	Au	Au, 20	glass	$Fe_{0.68}Au_{0.32}$
8	3.0 nm Fe/2.5 nm Au	20	Au	Au, 20	glass	$Fe_{0.63}Au_{0.37}$
9	3.0 nm Fe/3.0 nm Au	20	Au	Au, 20	glass	$Fe_{0.59}Au_{0.41}$

The parameters of the prepared MLF are shown in Tables 1 and 2.

The optical simulations need the knowledge of the optical and MO properties of the constituent sublayers of the MLF (as input parameters for simulation). Therefore, film and bulk samples of pure NM, $3d$-TM, Si as well as of nearly equiatomic $3d$-TM/NM alloys and several $3d$-TM-silicides films were additionally fabricated in the similar deposition conditions (for the film samples) and their DF were determined. It should be noted here that the films of $3d$-TM silicides were prepared also in crystalline and amorphous phases by using flash evaporation onto heated and cooled substrates, respectively.

The structural characterization of the prepared MLF and film samples was performed by using $\Theta-2\Theta$ high-angle x-ray diffraction (HAXRD) and low-angle x-ray diffraction (LAXRD) with CuK_α and CoK_α radiation.

The optical properties (the real and imaginary parts of the complex refractive index, $\widetilde{N} = n - ik$) of the samples were measured at RT in a spectral range of $260-1130$ nm ($4.7-1.1$ eV) at a fixed incidence angle of $73°$ by the polarimetric Beattie technique [45]. The obtained values of n and k were used for calculating the spectral dependence of the real (ε_1) and imaginary (ε_2) parts of the diagonal components of the DF tensor $\tilde{\varepsilon}_{xx} = \tilde{\varepsilon}_{yy} = \tilde{\varepsilon}_{zz} = \varepsilon_1 - i\varepsilon_2$, and also of the optical conductivity

TABLE 2. Parameters of the prepared $3d$-TM/Si MLF.

Sample No.	Nominal MLF formula	Nominal overall MLF stoichiometry	Numbers of bilayer repetitions	Top layer	Substrate	Ion-beam treatment	Temperature of heat treatment (K)
10	3.0 nm Ni/2.69 nm Si	$Ni_{0.67}Si_{0.33}$	40	Ni	Si	+	–
11	3.0 nm Ni/5.37 nm Si	$Ni_{0.50}Si_{0.50}$	50	Ni	Si	+	473, 673, 1073
12	3.0 nm Ni/10.7 nm Si	$Ni_{0.33}Si_{0.67}$	22	Ni	Si	+	473, 673, 1073
13	3.0 nm Ni/10.6 nm Si	$Co_{0.33}Si_{0.67}$	20	Co	Si	–	673, 873, 973, 1073
14	3.0 nm Fe/1.0 nm Si	$Fe_{0.84}Si_{0.16}$	50	Fe	glass	–	–
15	3.0 nm Fe/1.3 nm Si	$Fe_{0.80}Si_{0.20}$	50	Fe	glass	–	–
16	3.0 nm Fe/1.5 nm Si	$Fe_{0.77}Si_{0.23}$	50	Fe	glass	–	–
17	3.0 nm Fe/1.8 nm Si	$Fe_{0.74}Si_{0.26}$	50	Fe	glass	–	–
18	3.0 nm Fe/2.0 nm Si	$Fe_{0.72}Si_{0.28}$	50	Fe	glass	+	773
19	3.0 nm Fe/2.2 nm Si	$Fe_{0.70}Si_{0.30}$	50	Fe	glass	+	–
20	0.3 nm Fe/0.5 nm Si	$Fe_{0.50}Si_{0.50}$	120	Fe	glass	–	668, 748, 850

(OC, σ) by using the expressions: $\varepsilon_1 = n^2 - k^2$, $\varepsilon_2 = 2nk$, and $\sigma(\hbar\omega) = \dfrac{\varepsilon_2 \omega}{4\pi}$, where ω is the angular frequency of light.

The MO equatorial Kerr effect (EKE) of the samples was measured at RT by the dynamical method using the *p*-plane polarized light at two angles of incidence (66 and 75°) in a spectral range of 260–1130 nm (4.7–1.1 eV) and in an AC saturation magnetic field. The EKE value, $\delta_p = \Delta I / I_o$, is the relative change in intensity of the reflected light, caused by the magnetization of the sample in an external magnetic field directed transversely to the plane of the light incidence. The real (ε_2') and imaginary (ε_1') parts of the off-diagonal components of the DF ($\tilde{\varepsilon}_{xy} = -\tilde{\varepsilon}_{yx} = i\tilde{\varepsilon}'$, $\tilde{\varepsilon}' = \varepsilon_1' - i\varepsilon_2'$) for the investigated samples were determined by using the experimental results of the optical study and the MO measurements at two angles of incidence.

In-plane magnetization loops, $M(H)$, for the investigated MLF were measured by using a vibrating sample magnetometer (VSM). FMR spectroscopy at RT and higher temperatures was also employed for the magnetic study of the MLF.

After, the structural and physical properties of the as-deposited 3*d*-TM/Si MLF had been investigated, the MLF were ion-beam mixed in a high vacuum ($\sim 1 \times 10^{-6}$ Torr) by Ar$^+$ ions directed normally to the film surface at the following conditions: an ion energy of 80 keV, an ion flux of 1.5×10^{-6} A/cm^2, and an ion dose of 1.5×10^{16} Ar$^+$/cm^2. After mixing all the investigations were repeated.

Additionally to ion-beam treatment, some of the 3*d*-TM/Si MLFs were annealed at different temperatures in order to induce the solid-state reactions in it.

B. Simulation Details

The theoretical simulations of δ_p, σ and ε_1 spectra for various MLF were performed by solving exactly a multireflection problem by using the scattering matrix approach [46], assuming either 'sharp' (ideal) interfaces resulting in rectangular depth profiles of the components or 'mixed' (alloy-like) interfaces of variable thickness between pure sublayers. The number of the constituent sublayers, their nominal thickness and optical properties, and the angle of incidence were the input parameters for the simulation.

It is clear that for the case of the mixed interfaces in the A/B MLF, the transition from the A to B sublayer encounters a transitional region where the A_xB_{1-x} alloy concentration is gradually changed from a A-rich A_xB_{1-x} alloy to a B-rich A_xB_{1-x} alloy through the equiatomic $A-B$ region. More accurately, such an interfacial region

probably can be expressed by a set of $A_x B_{1-x}$ alloy planes of different compositions.

On the other hand, the thickness of this interfacial region cannot be larger than a half of the bilayer period, and usually does not exceed 1–2 nm, or 3–7 interatomic distances.

Additionally, the alloys of one or two monolayers' thick probably have no significant physical meaning for the relevant properties. Therefore, the equiatomic A–B alloy is considered as an idealized approximation representing the actual interface structure and simplifying the simulation of the optical and MO properties of the A/B MLF with mixed interfaces.

The complex DF $\hat{\varepsilon}$ for a magnetic medium magnetized along z-axis with three-fold or higher symmetry about z-axis has the following form

$$\hat{\varepsilon} = \begin{pmatrix} \tilde{\varepsilon}_{xx} & \tilde{\varepsilon}_{xy} & 0 \\ -\tilde{\varepsilon}_{xy} & \tilde{\varepsilon}_{yy} & 0 \\ 0 & 0 & \tilde{\varepsilon}_{zz} \end{pmatrix}, \tag{1}$$

where, in general, the diagonal and off-diagonal terms are complex. Introducing the complex Voigt parameter

$$\tilde{Q} = \frac{i\tilde{\varepsilon}_{xy}}{\tilde{\varepsilon}_{xx}}, \tag{2}$$

and assuming that, for polycrystalline materials, $\tilde{\varepsilon}_{xx} = \tilde{\varepsilon}_{yy} = \tilde{\varepsilon}_{zz}$, $\tilde{\varepsilon}_{xy} = i\tilde{\varepsilon}_{xx}\tilde{Q}$, and $\tilde{Q} = Q_1 - iQ_2$, we obtain

$$\hat{\varepsilon} = \tilde{\varepsilon}_{xx} \begin{pmatrix} 1 & -i\tilde{Q} & 0 \\ i\tilde{Q} & 1 & 0 \\ 0 & 0 & 1 \end{pmatrix}. \tag{3}$$

For a magnetically ordered medium in a magnetic field, the complex refractive indices for the left (–)- and right (+)-circularly polarized light can be defined as

$$\tilde{N}_{\pm}^2 = \tilde{\varepsilon}_{xx} \pm i\tilde{\varepsilon}_{xy} = \tilde{\varepsilon}_{xx}(1 \mp \tilde{Q}), \tag{4}$$

while, for a nonmagnetic medium, this expression can be transformed into

$$\tilde{N}^2 = \tilde{\varepsilon}_{xx} = \varepsilon_1 - i\varepsilon_2 = (n - ik)^2 = (n^2 - k^2) + i2nk. \tag{5}$$

C. Optical Properties of the MLF

Let us consider the MLF consisting of 1, 2, 3, ..., j, ..., m parallel, isotropic and homogeneous layers, which are put between a semi-infinite ambient medium (0) and a substrate $(m+1)$. The complex refractive indices of the medium and substrate are $\tilde{N}_0$ and $\tilde{N}_{m+1}$, respectively. Let $E^+(z)$ and $E^-(z)$ are the complex amplitudes of the electromagnetic wave, which propagates forward and back in an arbitrary plane z. E for different planes z' and z'' must be connected by the reorganization

$$\begin{pmatrix} E^+(z') \\ E^-(z) \end{pmatrix} = \begin{pmatrix} S_{11} & S_{12} \\ S_{21} & S_{22} \end{pmatrix} \begin{pmatrix} E^+(z') \\ E^-(z') \end{pmatrix}, \tag{6}$$

or, in a shorter way, Eq. (6) can be rewritten as

$$E(z^+) = SE(z''), \tag{7}$$

where S is the so-called scattering matrix

$$S = \begin{pmatrix} S_{11} & S_{12} \\ S_{21} & S_{22} \end{pmatrix}. \tag{8}$$

The scattering matrix S for such a MLF can be expressed as a result of the multiplication of the reflection and phase matrices, I and F, respectively, for each boundary and layer

$$S = I_{01} F_1 I_{12} F_2 \ldots I_{j(j+1)} F_{(j+1)} F_{(m+1)}. \tag{9}$$

The reflection matrix $I_{j(j+1)}$ describes the reflection between j-th and $(j+1)$-th adjacent layers,

$$I_{j(j+1)} = \frac{1}{T_{j(j+1)}} \begin{pmatrix} 1 & R_{j(j+1)} \\ R_{j(j+1)} & 1 \end{pmatrix}, \tag{10}$$

where the Fresnel coefficients of reflection and transmission between j and $j+1$ boundaries, $R_{j(j+1)}$ and $T_{j(j+1)}$, respectively, are calculated for the p- and s-polarizations by using the complex refraction index for j-th layer, $\tilde{N}_j = n_j - ik_j$:

$$R^p_{j(j+1)} = \frac{\tilde{N}_j^2 \tilde{A}_{j+1} - \tilde{N}_{j+1}^2 \tilde{A}_j}{\tilde{N}_j^2 \tilde{A}_{j+1} + \tilde{N}_{j+1}^2 \tilde{A}_j}, \qquad \tilde{T}^p_{j(j+1)} = \frac{2\tilde{N}_j \tilde{N}_{j+1} \tilde{A}_{j+1}}{\tilde{N}_j^2 \tilde{A}_{j+1} + \tilde{N}_{j+1}^2 \tilde{A}_j}, \tag{11}$$

and

$$R_{j(j+1)}^s = \frac{\tilde{A}_{j+1} - \tilde{A}_j}{\tilde{A}_{j+1} + \tilde{A}_j}, \qquad \tilde{T}_{j(j+1)}^s = \frac{2\tilde{A}_{j+1}}{\tilde{A}_{j+1} + \tilde{A}_j}, \qquad (12)$$

where $\tilde{A}_j = \sqrt{\tilde{N}_j^2 - \sin\varphi}$ and φ is the angle of incidence.

The phase matrix F_j for the j-th layer can be defined as

$$F_j = \begin{pmatrix} e^{i\delta_j} & 0 \\ 0 & e^{-i\delta_j} \end{pmatrix}, \qquad (13)$$

where $2\delta_j = \dfrac{4\pi d_j}{\lambda}\tilde{N}_j\cos\varphi$, d_j is the thickness of the j-th sublayer, and λ is the light wavelength. Thus, it is clear that the knowledge about the optical constants of each layer, the thickness and the angle of incidence are enough for calculating the resultant scattering matrix for the whole MLF.

After matrix S being calculated, the ellipsometric angles, ψ and Δ, for the whole MLF (as if the material is actually homogeneous) could be obtained by using the main equation of ellipsometry

$$\tan\psi \cdot e^{i\Delta} = \frac{S_{21}^p}{S_{11}^p}\frac{S_{11}^s}{S_{21}^s}. \qquad (14)$$

While the ellipsometric angles are determined by using Eq. (14), the effective optical constants, n_{eff} and k_{eff}, for the whole MLF can be calculated from the equations for the optical invariants

$$\varepsilon_{1(eff)} = n_{(eff)}^2 - k_{(eff)}^2 = \sin\varphi\left[1 + \tan^2\varphi\frac{\cos^2 2\psi - \sin^2 2\psi\sin^2\Delta}{(1 - \sin 2\psi\cos\Delta)^2}\right], \quad (15)$$

and

$$\varepsilon_{2(eff)} = 2n_{(eff)}k_{(eff)} = 2\sin^2\varphi\tan^2\varphi\left[\frac{\cos 2\psi\sin 2\psi\sin\Delta}{(1 - \sin 2\psi\cos\Delta)^2}\right]. \qquad (16)$$

D. Magnetooptical Properties of the MLF

According to Eq. (4), the complex refractive indices of each layer for the right- and left-circularly polarized light can be defined as

$$\tilde{N}_{+j}^2 = \tilde{\varepsilon}_{xxj}(1 - \tilde{Q}_j), \qquad (17)$$

$$\tilde{N}^2_{-j} = \tilde{\varepsilon}_{xxj}(1 + \tilde{Q}_j). \tag{18}$$

Using the same formalism, which was employed for the determination of the effective optical constants for the whole MLF, and Eqs. (17) and (18), the effective complex refractive indices for the left- and right-circularly polarized light can be determined, and then the effective diagonal and off-diagonal components of the DF can be obtained:

$$\tilde{\varepsilon}_{xx(eff)} = \frac{N^2_{(eff)+} + N^2_{(eff)-}}{2}, \tag{19}$$

$$Q_{(eff)} = \frac{N^2_{(eff)+} - N^2_{(eff)-}}{N^2_{(eff)+} + N^2_{(eff)-}}, \tag{20}$$

$$\tilde{\varepsilon}_{xy(eff)} = -i\tilde{\varepsilon}_{xx(eff)}\tilde{Q}_{eff}, \tag{21}$$

$$\varepsilon'_{1(eff)} - i\varepsilon'_{2(eff)} = \frac{N^2_{(eff)+} - N^2_{(eff)-}}{2}. \tag{22}$$

The transverse or equatorial Kerr effect for the whole MLF can be expressed as [47]:

$$\delta_p = 2\sin 2\varphi\left(\frac{\mathscr{A}\,\varepsilon'_{1(eff)}}{\mathscr{A}^2 + \mathscr{B}^2} + \frac{\mathscr{B}\,\varepsilon'_{2(eff)}}{\mathscr{A}^2 + \mathscr{B}^2}\right), \tag{23}$$

where

$$\mathscr{A} = \varepsilon_{2(eff)}(2\varepsilon_{1(eff)}\cos^2\varphi - 1),$$

$$\mathscr{B} = (\varepsilon^2_{2(eff)} - \varepsilon^2_{1(eff)})\cos^2\varphi + \varepsilon_{1(eff)} - \sin^2\varphi.$$

RESULTS AND DISCUSSION

A. MO and Optical Properties of Noble Metal/3d-TM Multilayers

As an example, the HAXRD and LAXRD spectra for the Fe/Au MLF (sample No. 7) are shown in Fig. 1. Several satellites are clearly seen in the LAXRD spectrum indicating well-layered structure of the Fe/Au MLF. The presence of a well-ordered layered structure is also supported by the presence of several Bragg satellites in the HAXRD
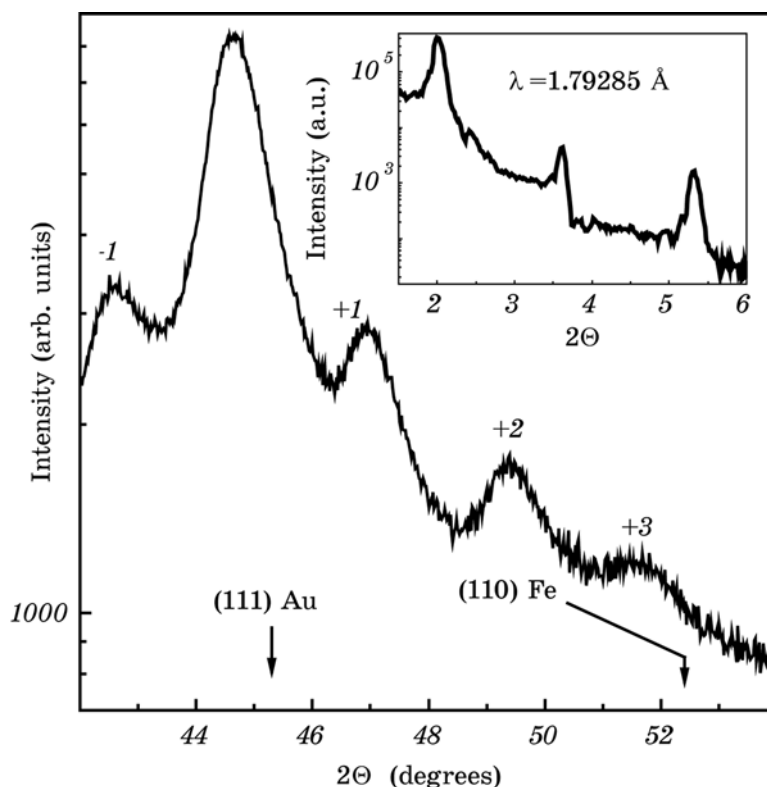
Fig. 1. HAXRD and LAXRD (see inset) spectra for the Fe/Au MLF (sample No. 7).

spectrum located symmetrically around main diffraction peak, which originates from the buffer layer. The calculation of the actual bilayer period of the Fe/Au MLF by using LAXRD as well as HAXRD satellite peak positions reveals the consistent results. An increase of the Au sublayer thickness causes the decrease in interval between satellites peaks in the LAXRD spectra and some shift of the main diffraction maximum to the high-angle side of the HAXRD spectra. From the HAXRD measurements a pronounced (111)-texture for the as-deposited Co/Pt MLF was inferred.

The in-plane magnetization hysteresis loops, $M(H)$, for the Fe/Au MLF taken at RT indicate their magnetically soft behaviour with a coercivity of about $10-16$ Oe and show the presence of the superparamagnetic behaviour in a high-field region. The superparamagnetic contribution was also observed for the field dependences of the EKE. Both these factors allow us to suppose that two magnetic phases are present in the Fe/Au MLF.

The measured optical properties of the Fe/Au MLF together with
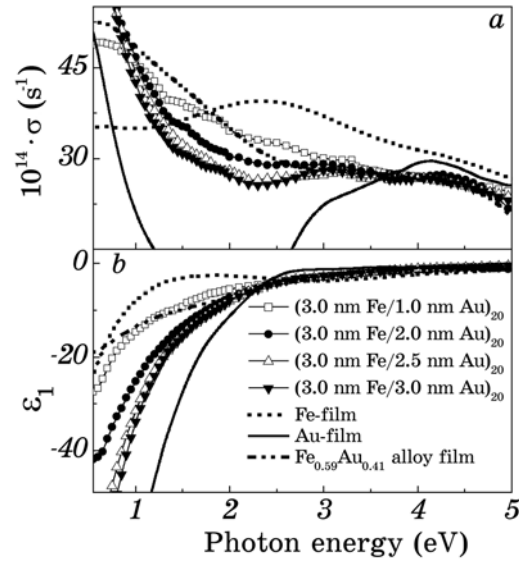
Fig. 2. The experimental (*a*) OC and (*b*) ε_1 spectra for the Fe/Au MLF together with those for Fe, Au and $Fe_{0.59}Au_{0.41}$ alloy films. The similar designations of the curves are used in panels (*a*) and (*b*).

those of Fe, Au and nearly equiatomic $Fe_{0.59}Au_{0.41}$ alloy films are shown in Fig. 2. The optical properties of gold are well known [48] and are explained by first-principles calculations [49]. The experimentally obtained $\sigma(\hbar\omega)$ and $\varepsilon_1(\hbar\omega)$ spectra for the Au-film nicely reproduce known literature results, namely a rapid break in the OC near 2.5 eV (which is related to the threshold of the interband absorption) and pure intraband absorption below $\hbar\omega < 2$ eV. The optical properties of the Fe-film are also in an agreement with known experimental [50] and theoretical [51] results, exhibiting a wide interband absorption peak in the OC spectrum near 2.4 eV. As a whole, the optical properties of the Fe/Au MLF manifest the optical properties of both Fe and Au. Since, however, the 2.4 eV peak of Fe is located practically at the same energy of deep minimum of the OC spectrum of Au, the resulting $\sigma(\hbar\omega)$ spectra of the Fe/Au MLF are free of any prominent features: a broad plateau of the $\sigma(\hbar\omega)$ is seen for the 2–5 eV energy range, while for $\hbar\omega < 1.5$ eV energy region intraband absorption becomes dominant. The optical properties of $Fe_{0.59}Au_{0.41}$ alloy films in the visible region of spectra are in between of pure Fe and Au ones being rather similar to those of the Fe/Au MLFs.

The $\sigma(\hbar\omega)$ and $\varepsilon_1(\hbar\omega)$ spectra of pure Co and Pt films, as well as of Co/Pt MLFs in the $0.5 < \hbar\omega < 5.0$ energy range do not show any significant peculiarity and practically monotonously increases in
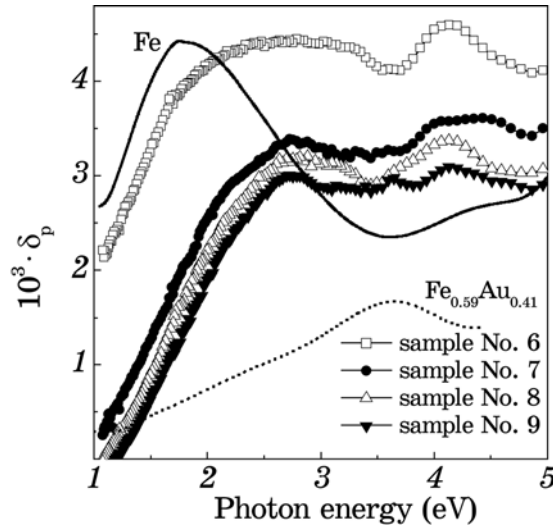
Fig. 3. EKE spectra for the Fe/Au MLF taken at RT and the angle of incidence of 66°. The EKE spectra for pure Fe (with a scaling factor of 0.5) and $Fe_{0.59}Au_{0.41}$ alloy films are shown for the comparison.

absolute value with decrease in photon energy. The only regularity can be mentioned: the $\sigma(\hbar\omega)$ and $\varepsilon_1(\hbar\omega)$ values for Pt film are always larger than the corresponding spectra of the Co-film, with $\sigma(\hbar\omega)$ and $\varepsilon_1(\hbar\omega)$ spectra for the Co/Pt MLFs in between of them (not shown). The experimental EKE spectra for Fe/Au MLFs as well as pure Fe and $Fe_{0.59}Au_{0.41}$ alloy films are shown in Fig. 3.

Since the differences between the experimental and simulated $\delta_p(\hbar\omega)$, $\sigma(\hbar\omega)$ and $\varepsilon_1(\hbar\omega)$ spectra turn out to be nearly the same for all the investigated Fe/Au MLF, we restrict our discussions on the sample No. 9 (see Figs. 4 and 5). Noticeable disagreements between the experimental and simulated $\delta_p(\hbar\omega)$, $\sigma(\hbar\omega)$ and $\varepsilon_1(\hbar\omega)$ spectra obtained for the model of nominal structure of Fe/Au MLF and abrupt interfaces between pure metal sublayers is a clear indication of bad approach used to model the MLF. Simultaneously the best correspondence between experimental and simulated $\sigma(\hbar\omega)$ and $\varepsilon_1(\hbar\omega)$ spectra in the whole spectral range was obtained for the MLF model of the sample No. 9, which supposes the formation of the alloyed interfacial region of $t_{int}(9) = 1.8$ nm in thickness between Fe and Au sublayers (see Fig. 4). The increase the thickness of the interfacial region in the model results in even worse fitting. The interfacial region was modelled by using the optical constants of the ferromagnetic $Fe_{0.59}Au_{0.41}$ alloy films. Nearly, the same thicknesses of the alloyed interfacial regions provide ($t_{int}(7) = 1.7$ nm; $t_{int}(8) = 1.9$ nm) also the best fit of the simulations for other Fe/Au MLFs, sample
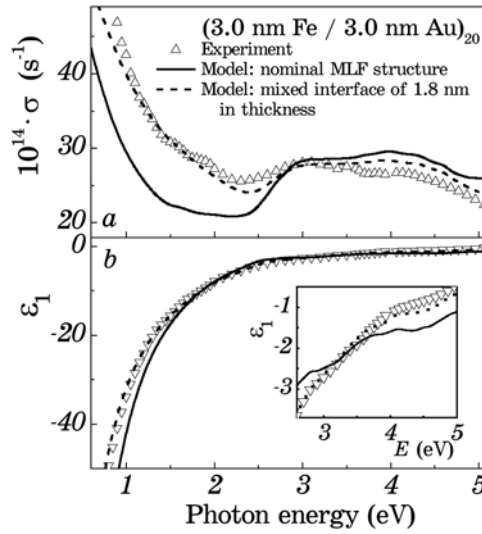
Fig. 4. Experimental (open triangles) and simulated (lines) (*a*) $\sigma(\hbar\omega)$ and (*b*) $\varepsilon_1(\hbar\omega)$ spectra for the (3.0 nm Fe/3.0 nm Au)$_{20}$ MLF obtained for the model of the nominal MLF structure (solid lines) and for the case of mixed interface of 1.8 nm in thickness between Fe and Au layers (dashed lines). Inset in panel (*b*) shows an enlarged view of the high-energy part of the $\varepsilon_1(\hbar\omega)$ spectra.
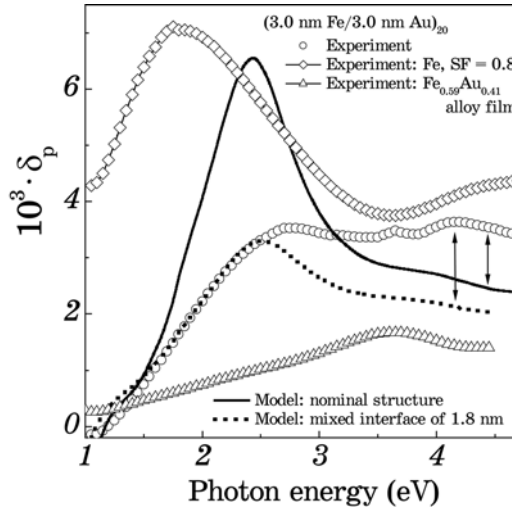
Fig. 5. Experimental (symbols) and simulated (lines) EKE spectra for the (3.0 Fe/3.0 nm Au)$_{20}$ MLF obtained for the model of the nominal MLF structure and for the case of mixed interface of 1.8 nm in thickness between Fe and Au layers. The experimental EKE spectrum for Fe-film is shown by open diamonds for the comparison.

Nos. 7 and 8. It should be reminded here, that in optical simulations we used the optical constants of 'thick' (~ 100 nm or more) Fe, Au and $Fe_{0.59}Au_{0.41}$ films and obtained reasonable correspondence between experiment and simulations in the whole investigated spectral range. This means that the optical properties (and hence the electronic structures) of the 'thin' ($\sim 1-3$ nm in thickness) Fe and Au layers in Fe/Au MLF are close to those of 'bulk' Fe and Au; no 'quantum well states' were detected in the investigated Fe/Au MLF in such a way.

It is seen (see Fig. 3) that the experimental EKE spectra for Fe/Au MLF are characterized by two peculiarities (or peaks) which are located at $\sim 2.7-2.8$ and ~ 4 eV. At the same time, the EKE spectrum for pure Fe-film exhibits a definite maximum at ~ 1.7 eV. The comparison between the experimental and simulated EKE spectra for the Fe/Au MLF allow us to conclude that the low-energy peak in the EKE of the Fe/Au MLF originates from Fe-sublayers and its blue-shift by about 1 eV is caused by the interplay of the optical constants in the Fe/Au MLF. Indeed, the modelled EKE spectrum obtained for the model of the nominal Fe/Au MLF structure and nonmagnetic Au sublayers, exhibits a strong peak which is located at practically the same energies as the experimental one (see Fig. 5). At the same time such a simulation reveals that the experimental EKE spectrum exceeds the modelled one for $\hbar\omega > 3.0$ eV. The simulation of the EKE spectra for the Fe/Au MLF model with alloyed interfacial region of the same thickness (which allowed to obtain best resemblance of the experimental and simulated optical spectra), reveals perfect fit to the experimental data in low-energy region. As input parameters for alloyed interfacial regions in this model of Fe/Au MLF, the MO and optical properties of the ferromagnetic $Fe_{0.59}Au_{0.41}$ alloy film were used. However, for $\hbar\omega > 2.5$ eV energy range, the experimental MO response still exceeds the modelled one. Thus, it is clear that, in addition to ferromagnetic Fe and $Fe_{0.59}Au_{0.41}$ sublayers, the presence of the third source in the resulting MO response of the Fe/Au MLF should be supposed. Moreover, this source may be spin-polarized Au sublayers [52].

In order to determine the MO properties (*i.e.* the off-diagonal components of the DF tensor) of spin-polarized Au layers, the following approach was employed. All the experimental responses which exceed the modelled one (for alloyed interface model) one, *i.e.*, $\Delta(\hbar\omega) = \delta_{p\_exp.}(\hbar\omega) - \delta_{p\_mod.}(\hbar\omega)$ was determined at two angles of incidence (*i.e.*, at $\varphi = 66$ and $75°$) and referred to as the spin-polarized Au sublayers. Having known the optical constants of Au layers and the $\Delta(\hbar\omega)$ at two angle of incidence, the absorptive $(\hbar\omega)^2\varepsilon'_2$ and dispersive $(\hbar\omega)^2\varepsilon'_1$ parts of the off-diagonal components of the DF for spin-polarized Au sublayers were determined by using the algorithm
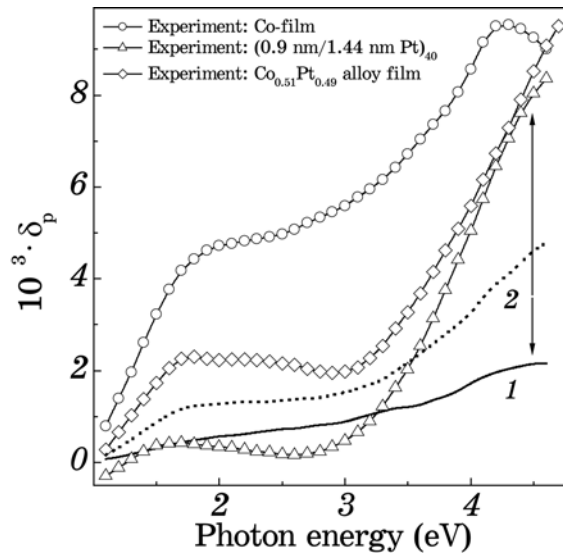
Fig. 6. Experimental (symbols) and simulated (lines) EKE spectra for the $(0.9 \text{ nm Co}/1.44 \text{ nm Pt})_{40}$ MLF obtained for the model of the nominal MLF structure (solid line) and for the case of mixed interface of 0.9 nm in thickness between Co and Pt layers (dashed line). The EKE spectra for pure Co and $Co_{0.51}Pt_{0.49}$ alloy films are shown for the comparison.
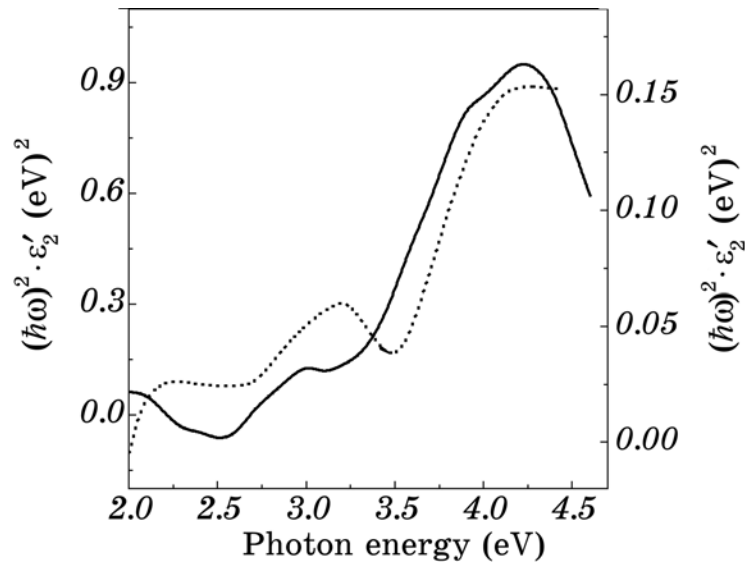
Fig. 7. Absorptive parts of the off-diagonal components of the DF for spin-polarized Pt (solid line, left scale) and Au (dashed line, right scale) layers.

of Krinchik [47]. Practically the same regularities between experimental and simulated EKE spectra were also observed for Co/Pt MLF (see Fig. 6). The detailed results related to Co/Pt MLF can be found elsewhere [53]. Figure 7 shows the $(\hbar\omega)^2\varepsilon'_2$ spectra for Pt and Au layers obtained in such a way. Both these spectra manifest a prominent peak near 4 eV (while the magnitude of Au-related peak is much smaller) and this fact explains large experimental MO responses in the UV region of spectra observed for Co/Pt and Au/Fe MLFs.

B. Interlayer Coupling in the Fe/Si MLF

HAXRD spectra of the all as-deposited Fe/Si MLFs (sample Nos. 14−19) look rather similar to each other with small differences in main diffraction peak position. As an example, one of them (related to the sample No. 18) is shown in Fig. 8. The asymmetry of the satellite peak with respect to the main peak in the HAXRD spectra for the Fe/Si MLF has been also observed earlier by Chaiken *et al.* [37] and Fullerton *et al.*, and explained by the presence of interdiffused interfaces [36]. No peak related to Si or other elements was
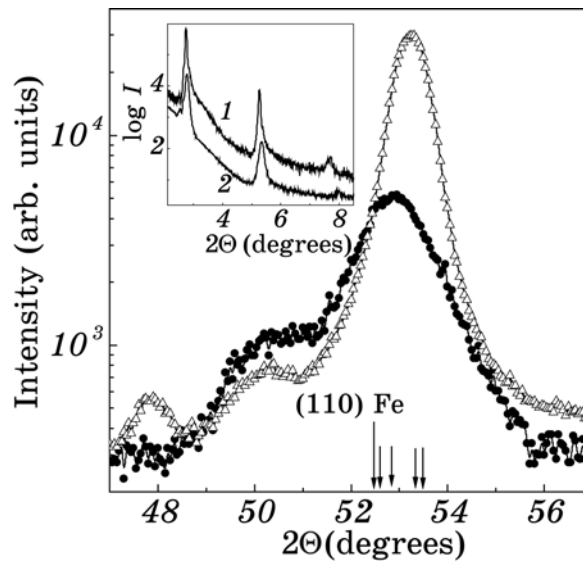
Fig. 8. HAXRD and LAXRD (see inset) spectra for the Fe/Si MLF (sample No. 18) in the as-deposited state (solid circles and 1) and after ion-beam treatment (open triangles and 2). Arrows show the position of the most intense diffraction lines for Fe and (from left to right) for crystalline silicides of Fe_2Si, ε-FeSi, Fe_5Si_3 and Fe_3Si, respectively.

found. The Fe/Si MLF manifests a crystal coherence length, ξ, estimated from the FWHM of the main diffraction peak, of about 7 nm. This implies that there is no amorphous Si left in our samples and the interfacial reaction between Si and Fe has led to a crystalline multilayer structure. The main diffraction peak is located near the (110)Fe peak location as well as near the positions of the most intense diffraction lines for several stable at RT iron silicides (see Fig. 8). Therefore, having only the HAXRD data it is hard to conclude definitely what structure the as-deposited Fe/Si MLF has. At the same time, the LAXRD patterns for the as-deposited Fe/Si MLF confirm their layered structure (see inset in Fig. 8).

The prepared Fe/Si MLFs exhibit the fairly strong AF coupling, as already reported [35, 37, 43]. The saturation field H_s for in-plane hysteresis loops of the $(3.0 \text{ nm Fe}/m \text{ Si})_{50}$ MLFs, where m is the Si-sublayer thickness, rapidly increases from 0.08 kOe for $m = 1.0$ nm reaching the peak value of $H_s \sim 12-14$ kOe at $m = 1.3$ nm, and then decreases down to 0.2 kOe for $m = 2.2$ nm, indicating a strong AF exchange coupling.

As aforementioned for the purpose of simulations, the optical properties of nominal and possible candidates for the constituent sublayers of Fe/Si MLF, $i.e.$, of Fe, Si, and amorphous $FeSi_2$ films as well as α-$FeSi_2$, β-$FeSi_2$, and ε-FeSi bulks, were measured (not shown). It should be mentioned here that all the examined candidates for the spacer (except, naturally, Fe) show a large and positive ε_1 in the IR region of spectra and a relatively small σ, in other words, exhibit a semiconductor-like behaviour. Knowing the optical characteristics of these materials, we can calculate the MO and optical properties of the Fe/Si MLF and compare the simulated spectra with the experimentally determined ones.

Since the observed regularity in the behaviour of the experimental and simulated $\delta_p(\hbar\omega)$, $\sigma(\hbar\omega)$ and $\varepsilon_1(\hbar\omega)$ spectra turn out to be nearly the same for all the investigated Fe/Si MLF, we restrict our discussions on sample No. 18 (see Fig. 9). First of all, two main results should be noted here; (i) the simulation with the nominal Fe/Si MLF structure predicts a prominent enhancement of the MO response in the near-IR region with respect to that of pure Fe; (ii) a decisive disagreement between the experimental and simulated $\delta_p(\hbar\omega)$ and optical spectra is observed for the case of the nominal structure of MLF in the model.

The enhancement of the MO response in the modelled EKE spectrum can be explained by an interplay between the optical constants of Fe and Si in this spectral range [see expression (23)]. The decisive disagreement between the experimental and the simulated (with the nominal Fe/Si MLF structure) $\delta_p(\hbar\omega)$, $\sigma(\hbar\omega)$ and $\varepsilon_1(\hbar\omega)$ spectra (see Fig. 9) suggests a presence of another than nominal layered structure in our as-deposited Fe/Si MLF.
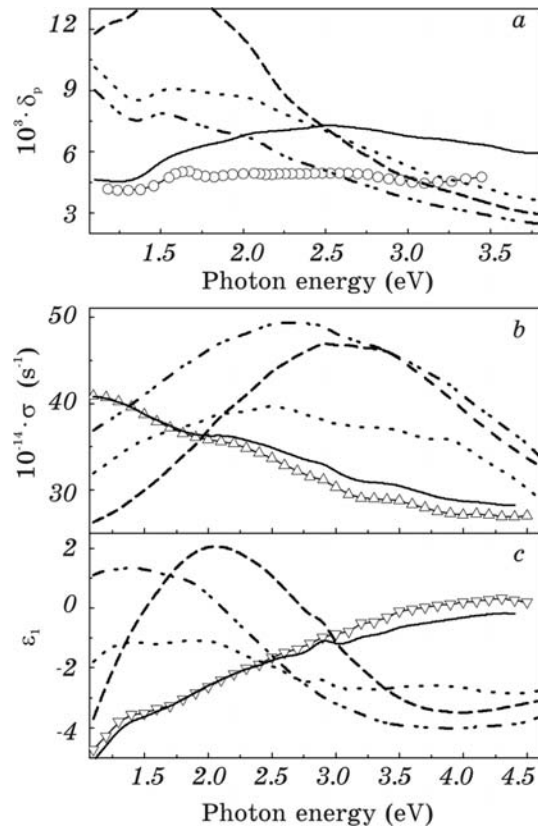
Fig. 9. Experimental (symbols) and simulated (lines) (*a*) $\delta_p(\hbar\omega)$ (*b*) $\sigma(\hbar\omega)$ and (*c*) $\varepsilon_1(\hbar\omega)$ spectra for (3.0 nm Fe/1.8 nm Si)$_{50}$ MLF. Various kinds of spacers were used in the simulations: (dashed lines) nominal MLF structure and amorphous Si, (dotted lines) amorphous FeSi$_2$, (dashed-dotted lines) ε-FeSi. Modelled spectra with use of extracted FeSi spacer are shown by solid lines.

Therefore, next step of simulations employed the Fe/Si MLF model, which supposes that all the Si sublayers were completely consumed for the formation of iron silicide of various stoichiometries. It should be reminded here that the spacer should be nonmagnetic. Therefore, the stoichiometry of the possible silicides as a spacer, *i.e.* Fe$_x$Si$_{1-x}$, should be searched in the $x \leq 0.5$ region. The thicknesses of the residual Fe sublayers and as well as of newly formed iron silicide sublayers for these models were calculated with use of the tabulated densities of crystalline iron silicides. The $\delta_p(\hbar\omega)$, $\sigma(\hbar\omega)$ and $\varepsilon_1(\hbar\omega)$ spectra for different models of the Fe/Si MLF are shown in Fig. 9. All these spectra appear to be completely different in both intensity and shape from the corresponding experimental ones.

Thus, such a decisive disagreement rules out the hypothesis of $FeSi_2$ or ε-FeSi silicides as spontaneously formed nonmagnetic spacers between Fe sublayers.

Because of lack of the knowledge of the optical properties of other iron silicides, we used another approach in order to determine the optical properties of the interfacial regions. We assumed that the experimentally observed optical properties of the Fe/Si MLF result from those of the Fe layers (whose optical properties are known) and of those of the hypothetical nonmagnetic spacers. Then, taking into account the additive character of the contributions from different phases to the DF of MLF, the optical properties of the spacer were extracted in the framework of the effective medium approximation for a spacer stoichiometry of FeSi. The correctness of such a procedure was cross-checked by employing the extracted optical properties of the spacer as input parameters in the reciprocal exact simulation that should restore the measured optical properties of the Fe/Si MLF. It is seen in Fig. 9, b and c that the simulated $\sigma(\hbar\omega)$ and $\varepsilon_1(\hbar\omega)$ spectra reproduce the experimental ones with a great resemblance.

In contrast to the cases based on the structural model with $FeSi_2$ or ε-FeSi as the spacers, the above approach allows us to obtain a significantly better correspondence in shape between experimental and simulated EKE spectra (see Fig. 9, a). However, it should be noted that the intensity of the modelled spectra is somewhat larger than the experimental one. The better resemblance in the intensity between experimental and simulated EKE spectra can be probably obtained by a more correct estimation of the fraction of nonreacted Fe in the actual Fe/Si MLF. The major finding is that the experimentally extracted optical properties of the spacer with FeSi stoichiometry exhibit rather similar energy dependence for all the examined Fe/Si MLF and possess a typical metallic behaviour (see Fig. 10) in contrast to $FeSi_2$ or ε-FeSi. Thus, such an approach leads us to suggest that the nonmagnetic spacer in the Fe/Si MLF, providing an AF coupling, is metallic with composition close to FeSi.

In order to understand the experimentally extracted optical properties of the spacer we calculated the electronic band structures of the FeSi compound with $B2$ type of structure using a scalar-relativistic version of tight-binding linear muffin-tin-orbital method within the local-spin-density approximation (LSDA). An atomic-sphere approximation was used. The spin-orbit interactions were included in the self-consistent iterations. For the exchange-correlation effect, we used the LSDA expression of von Barth and Hedin [54]. Once the self-consistent potential and charge were obtained, the density-of-states curves and the optical conductivity spectra were calculated using the linear-energy-tetrahedron method [55] with a finer mesh of irreducible wedge.
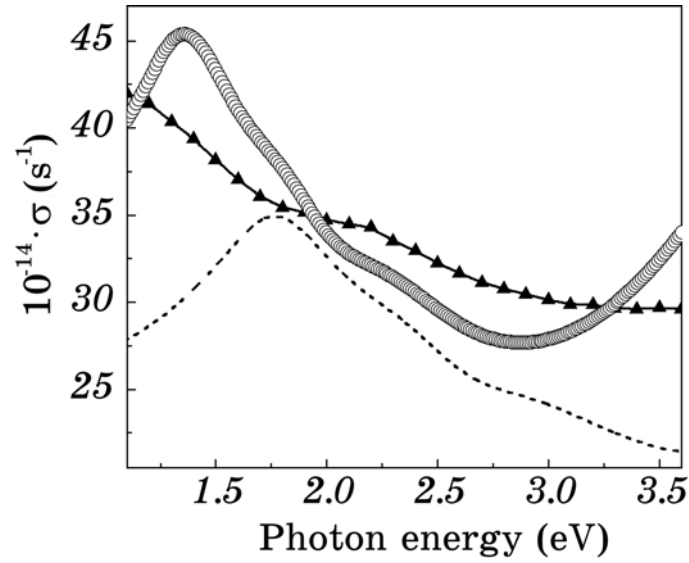
Fig. 10. Experimental (solid triangles) OC spectrum for the ion-beam treated (3.0 nm Fe/2.0 nm Si)$_{50}$ MLF together with calculated and broadened (dashed line) and self-energy corrected OC (open circles) spectra.

Figure 10 compares the theoretical $\sigma(\hbar\omega)$ spectra for FeSi with the extracted σ spectra of the spacer. Since the calculated and broadened σ spectrum for FeSi resembles the experimentally extracted one except the peak positions, we applied the real part of the self-energy correction (SEC) or λ-fitting [56] to match their energy positions. It is seen in Fig. 10 that the broadened and SEC σ spectrum for FeSi exhibits a noticeable resemblance to the experimentally extracted σ spectrum for the spacers. Therefore, it can be concluded that the metallic, nonmagnetic FeSi with a *B*2 structure is formed spontaneously in the Fe/Si MLF with relatively 'thick' sublayers.

Since such a spacer is spontaneously formed between Fe sublayers of Fe/Si MLF, we tempted to fabricate pure iron-silicide with *B*2-type of structure by choosing of proper Fe and Si sublayer thicknesses (sample No. 20, see Table 2). However, in spite of our expectations, the optical properties of the as-deposited and all the annealed Fe/Si MLF with 'thin' sublayers and overall composition of Fe$_{0.50}$Si$_{0.50}$ drastically differ from those of the aforementioned silicide spacer being rather similar to ε-FeSi ones. Even though the XRD spectra for this Fe/Si MLF in the as-deposited state after all steps of annealing indicate their amorphous structures, it can be supposed that the short-range order in such films is close to ε-FeSi, *i.e.*, to *B*20 type.

C. Optical Study of 3d-TM-Silicides Formation

Unlike the Fe/Si MLF case (sample Nos. 14–19, see Fig. 8) there are no any visible rings (peaks) in the HAXRD patterns for all the as-deposited Ni/Si and Co/Si MLFs (samples 10–13) (not shown). However, such amorphous-like structures are not homogeneous, since the corresponding LAXRD patterns exhibit several well-defined satellites, which indicate their good-layered structures (not shown). Also unlike the Fe/Si MLFs, the in-plane and out-of-plane magnetization hysteresis loops, $M(H)$, for all the as-deposited Ni/Si and Co/Si MLFs show the superparamagnetic behaviour. These results can be understood if the noticeable intermixing of the Ni(Co) with Si sublayers will be supposed. According to the results of Fallon [57] and Babu [58], the superparamagnetic behaviour at RT in co-deposited $Co_{1-x}Si_x$ and $Ni_{1-x}Si_x$ alloy films is observed for $x > 0.40$ and $x > 0.13$, respectively. The magnetic data obtained by VSM also corresponds to the results of the EKE measurements—no MO response at RT was detected for all the as-deposited Ni/Si and Co/Si MLFs. This allows us to assume that Ni and Co sublayers lost their ferromagnetic order owing to their enrichment by Si at least up to 13 and 40 at.%, respectively, and hence that the actual structures of the as-deposited MLFs are far from the nominal ones.

The shape of the simulated OC spectra of the Ni/Si and Co/Si MLFs (for the case of nominal MLF structures) is dictated by very intense absorption peak in OC spectrum of amorphous Si. All the simulated OC spectra for the Ni/Si MLF (see Fig. 11 and also, for Co/Si MLF, see Fig. 12) look rather similar each other in shape with some difference in peak position: an increase in Si sublayer thickness causes the red-shift of the maximum from ~3.30 (for the sample No. 10) to ~3.10 eV (for sample No. 12). The absence of even any visible trace of the Si-related absorption peak in the experimental OC spectra of the as-deposited Ni/Si MLF with overall stoichiometries of Ni_2Si and $NiSi$ as well as of Co/Si MLF enables us to suppose the lack (or a noticeable reduction) of the pure Si content in such films due to the Si (and naturally the Ni(Co)) consumption for the Ni(Co)-silicide formation. It is also seen that more or less reasonable correspondence in the shape between the simulated and experimental OC spectra is observed only for the Ni/Si MLF with the thickest (among the investigated Ni/Si MLF) Si sublayers (see Fig. 11, d). However, the magnitude of the modelled OC spectrum is larger than that of the experimental one. Thus, we can conclude that the employed MLF model, assuming the nominal MLF structures with an abrupt interfaces between pure Ni(Co) and Si sublayers does not describe adequately the actual structures of the as-deposited MLFs.
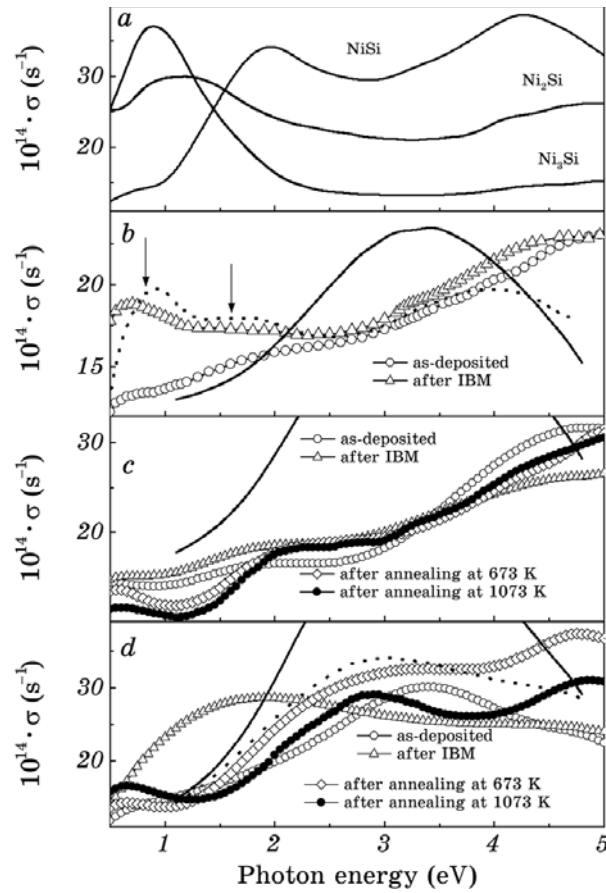
Fig. 11. Experimental (symbols) and modelled (lines) OC spectra for the as-deposited, ion-beam treated and annealed (b) (3.0 nm Ni/2.69 nm Si)$_{40}$, (c) (3.0 nm Ni/5.37 nm Si)$_{50}$ and (d) (3.0 nm Ni/10.7 nm Si)$_{22}$ MLFs. Solid lines on panels (b)−(c) represent the modelled OC spectra obtained for nominal MLF structures and shown with a scaling factors of 0.6, 1 and 1, respectively. Dashed lines on panels (b) and (d) show the modelled OC spectra obtained for the models with mixed interface (see text). Panel (a) shows the literature OC spectra for the crystalline nickel silicides [59].

Fortunately, unlike the case of the Fe/Si MLF, the OC spectra of the equiatomic as well as Ni-rich and Co-rich silicides are known from the literature [59] and from our measurements. All these spectra exhibit well definite absorption peaks located at noticeably different energies (see Figs. 11, *a* and 12, *a*). Comparing the experimental OC spectra for the as-deposited Ni/Si and Co/Si MLFs with those of aforementioned silicides, rough conclusion on the structures of the as-deposited and treated Ni/Si and Co/Si MLF can be
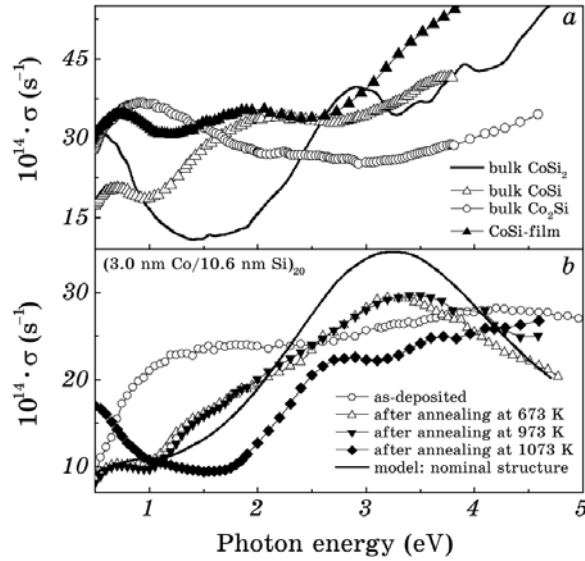
Fig. 12. Experimental OC spectra for (*a*) crystalline Co_2Si, CoSi and $CoSi_2$ silicides and (*b*) for the (3.0 nm Co/10.6 nm Si)$_{20}$ MLF in the as-deposited state and after several steps of annealing. For the convenience of the observation, OC for bulk Co_2Si is shifted downward by 7 units. Solid line on panel (*b*) represents the simulated OC spectrum for the nominal structure of the MLF shown with a scaling factor of 0.6.

made. Thus, noting that the OC spectra for the as-deposited Ni/Si MLFs (sample Nos. 10 and 11) have a peculiarities (or shoulders) at ~ 2 eV where the intense peak in the OC spectrum for crystalline equiatomic NiSi is located, the formation of the regions with the short-range order close to that presented in the η-NiSi may be supposed for such a MLF (see Fig. 11, *a–c*).

The agreement between the simulated and experimental OC spectra of the as-deposited (3.0 nm Ni/10.7 nm Si)$_{22}$ MLF is significantly improved in spectral shape and magnitude if the complete consumption of the Ni sublayers and hence a noticeable part of the Si sublayers for the formation of nonferromagnetic Ni-silicides of NiSi and Ni_3Si stoichiometries is assumed. The nearest approach to the experimental results was obtained for the model of this MLF with following sequence of the layers: (4.3 nm NiSi/1.2 nm Ni_3Si/4.7 nm Si/4.3 nm NiSi)$_{22}$ (see Fig. 11, *d*). As input parameters for Ni_3Si and amorphous NiSi, the literature results for crystalline Ni_3Si [59] as well as our experimental data for the as-deposited (3.0 nm Ni/5.37 nm Si)$_{50}$ MLF were used, since the latter one has an overall stoichiometry of NiSi and its optical properties are very close to those of crystalline NiSi (see Fig. 11, *a* and *c*). The spectral shape of the as-deposited Co/Si

MLF may be reasonably reproduced by the model, which supposes that the actual structure contains the regions with the short-range order close to Co_2Si (60%), CoSi (30%), and Si (10%).

IBM of the samples Nos. 10, 12, 18 and 19 does not produce any visible changes in the LAXRD spectra; HAXRD patterns for the Ni/Si MLF still indicate their amorphous structures, while HAXRD spectrum for the Fe/Si MLF is somewhat changed: main peak is shifted to the high-angle side, and becomes narrower and more intense (see Fig. 8). Again, because of several stable at RT iron-silicides have the most intense diffraction lines at the angles where main diffraction peak for the ion-beam treated Fe/Si MLF is located, any confident conclusion on the structure produced by IBM can be made on the basis of the HAXRD results.

However, the noticeable changes were observed in the OC spectra of the Ni/Si and Fe/Si MLF (see Figs. 11 and 13). Furthermore, the magnetic and MO measurements indicate that the IBM forms new magnetically soft phase with a smaller magnetization (see Fig. 14).

The OC spectrum of the ion-beam mixed (3.0 nm Ni/2.69 nm Si)$_{40}$ MLF shows a prominent enhancement in the magnitude for $\hbar\omega < 2.8$ eV, clearly revealing new absorption peaks at $\hbar\omega \sim 0.7$ and 1.8 eV (marked by arrows in Fig. 11, b). A comparison of the OC spectrum
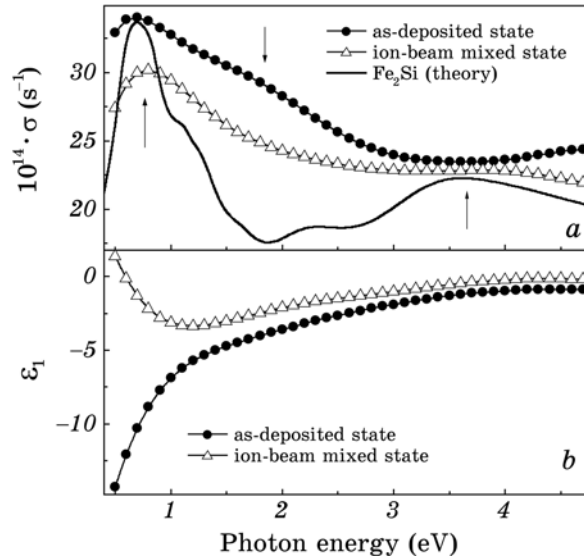
Fig. 13. (a) $\sigma(\hbar\omega)$ and (b) $\varepsilon_1(\hbar\omega)$ spectra for the as-deposited (solid circle) and ion-beam mixed (open triangles) (3.0 nm Fe/2.0 nm Si)$_{50}$ MLF. Solid line in (a) shows the broadened and self-energy corrected theoretical $\sigma(\hbar\omega)$ for Fe_2Si silicide ($B2$ type of structure). The theoretical $\sigma(\hbar\omega)$ spectrum is plotted with a scaling factor of 0.83.
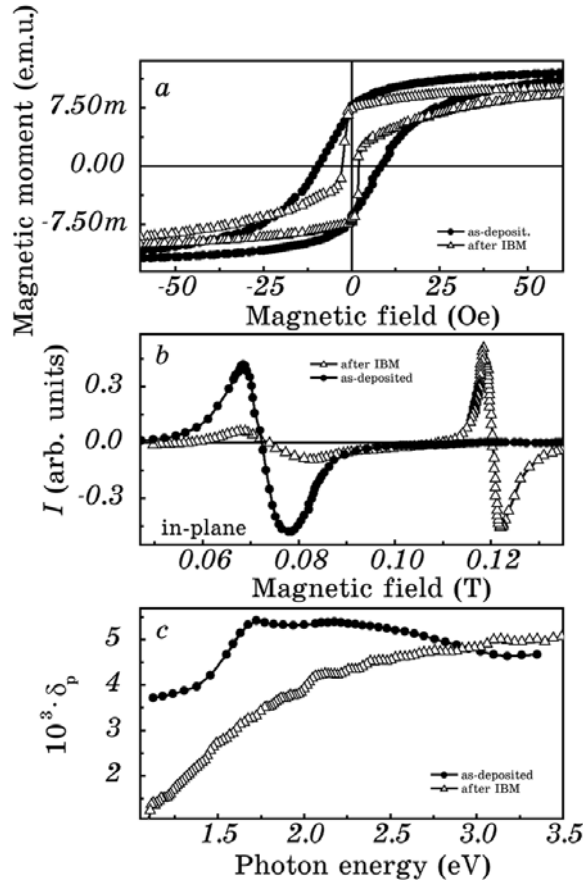
Fig. 14. (*a*) Magnetization hysteresis loops, (*b*) FMR and (*c*) EKE spectra for the (3.0 nm Fe/2.0 nm Si)$_{50}$ in the as-deposited state (solid circles), after ion-beam mixing (open triangles).

with those of various crystalline Ni silicides allows us to assume that the peak at ~1.8 eV is probably related to the low-energy peak in the OC spectrum of crystalline NiSi, while the 0.7 eV one originates from Ni$_2$Si or, more probably, from Ni$_3$Si. This supposition is further supported by the comparison of the experimental OC spectra with the simulated one made for the model with alloyed interfacial region (see Fig. 11, *b*). In this model, the following periodic element of the (3.0 nm Ni/2.69 nm Si)$_{40}$ MLF was used: (2.1 nm Ni/0.2 nm Ni$_3$Si/3.3 nm NiSi/0.2 nm Ni$_3$Si). As input parameters for simulation the optical constants for crystalline Ni$_3$Si [59] and as-deposited Ni/Si MLF of NiSi stoichiometry were used. The prominent changes in the OC spectra, induced by IBM, is also observed for the (3.9 nm Ni/13.9 nm Si)$_{22}$ MLF which can be interpreted in terms of a forma-

tion of the structures with a short-range order close to the mixture of Ni_2Si and NiSi (compare the corresponding OC spectra in Fig. 11).

Contrary to the aforementioned Ni/Si MLF, IBM does not produce any visible change in the OC spectrum of $(3.0\ nm\ Ni/5.37\ nm\ Si)_{50}$ MLF with an overall stoichiometry of NiSi: the spectrum after IBM (as well as as-deposited Ni/Si MLF) shows an absorption peak at $\hbar\omega \sim 2$ eV. Such a peak is absent in the OC spectra of pure Ni and Si, but is present in that of crystalline NiSi (see Fig. 11, *a*). Clevenger and Thompson revealed the experimental and thermodynamical evidences that the reaction phase selection in a polycrystalline Ni/amorphous Si thin film is governed by the so-called 'nucleation model': the formed silicide phase is one with the highest nucleation rate or the smallest nucleation barrier [60]. Therefore, it can be assumed that the nuclei of NiSi phase (for example, amorphous NiSi) are spontaneously formed during the deposition of $(3.0\ nm\ Ni/5.37\ nm\ Si)_{50}$ MLF, and IBM does not produce new ones.

The stoichiometry of the ion-beam mixed layers can be also qualitatively estimated by comparing the experimentally determined optical properties of Fe/Si MLF after the IBM with those of Fe–Si alloys of various compositions. It is seen that the calculated (broadened and self-energy corrected) OC spectrum for Fe_2Si silicide (a $B2$ type of structure) presents a reasonable resemblance to the experimental OC spectrum of Fe/Si MLF after the IBM in both shape and location of the absorption peaks (see Fig. 13, *a*). The electronic energy band structures of Fe_2Si silicide were calculated using a scalar-relativistic version of atomic-sphere-approximation tight-binding linear-muffin-tin-orbital method within the local-spin-density-approximation [61]. Since the stoichiometry of Fe_2Si alloy is not appropriate for the equilibrium $B2$-type structure (because a half of the Si sites should be unoccupied in this case), we assumed that a vacancy is introduced in the formula unit, and 2 Fe atoms, 1 Si atom and 1 vacancy form a Heusler-like alloy; *i.e.* a chain of Fe–Si–Fe-vacancy is aligned along the (111) direction of the $B2$-type unit cell. The resultant Bravais lattice is f.c.c. The details for calculation of the optical properties and for use of the self-energy correction can be found elsewhere [62].

According to the results of HAXRD study, an annealing of the Ni/Si and Co/Si MLFs (sample Nos. 11–13) at 673 K leads to the appearance of weak traces of the intermediate phases, *i.e.* of η-NiSi as well as Co_2Si and mainly CoSi, respectively. Next steps of annealing of the Co/Si MLF at 873 and 973 K cause the formation of the CoSi phase, while annealing at 1073 K forms $CoSi_2$ phase in Co/Si MLF. An annealing at temperatures of 873 K and 1073 K of the $(3.0\ nm\ Ni/5.37\ nm\ Si)_{50}$ MLF does not cause any difference in the HAXRD patterns. However, an annealing at 1073 K of the (3.0 nm

Ni/10.7 nm Si)$_{22}$ MLF leads to appearance additionally of the only (111) NiSi$_2$ diffraction line. Thus, according to the HAXRD results, the (3.0 nm Ni/5.37 nm Si)$_{50}$ MLF is crystallized into the η-NiSi phase, while the annealing at 1073 K of the (3.0 nm Ni/10.7 nm Si)$_{22}$ MLF leads to the formation of a dual structure (a mixture of η-NiSi and NiSi$_2$) with a predominance of the η-phase. It should be mentioned here that the observed sequence of the Ni-silicide phases, induced by the thermal annealing, in the investigated Ni/Si MLF differs from those in the literatures: an annealing at 1073 K of the Ni/Si layered structure usually leads to the NiSi$_2$ phase [22, 24, 25]. Thermal annealing at different temperatures (above 473 K) of the (3.0 nm Ni/5.37 nm Si)$_{50}$ causes gradual changes in the optical properties towards those of the crystalline NiSi: each step of annealing makes the interband absorption peak at $\hbar\omega \sim 2$ eV more evident. This means that such a process illustrates an improvement in the crystallinity of NiSi phase spontaneously formed during the film deposition. Contrary to the HAXRD results, the evolution of OC spectrum, induced by the thermal annealing of the (3.0 nm Ni/10.7 nm Si)$_{22}$ MLF above 473 K, clearly indicates the formation of NiSi$_2$ phase. The optical and HAXRD results might be correlated when we take into account the fact that the skin depth for the visible region is about 20 nm and also that the formation of NiSi$_2$ phase takes place mainly in the surface region of MLF, while the HAXRD response is
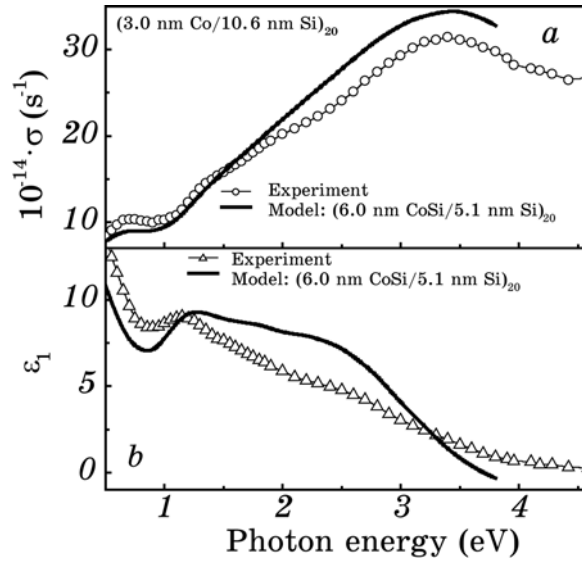
Fig. 15. Experimental (symbols) and simulated (solid lines) (*a*) OC and (*b*) $\varepsilon_1(\hbar\omega)$ spectra for the (3.0 nm Co/10.6 nm Si)$_{20}$ MLF after annealing at 873 K. The simulated OC spectrum is plotted with SF of 0.66.

made from the total volume of MLF.

The comparison of the experimental optical properties of the (3.0 nm Co/10.6 nm Si)$_{20}$ MLF subjected to the annealing at 873 K allows us to conclude that newly formed CoSi phase as well as residual Si are main components of the Co/Si MLF (see Fig. 15). An annealing of the Co/Si MLF at 1073 K causes the prominent changes in its optical properties: the interband absorption peaks at 0.7 and 1.5−2 eV have disappeared, and instead of a broad peak at 3.2 eV, two peaks at 2.75 and 3.6 eV have occurred in the OC spectrum of this MLF (see Fig. 12). The comparison of the experimental σ spectrum of such an annealed Co/Si MLF with that of crystalline bulk CoSi$_2$ (see Figs. 12, *a* and *b*) indicates their perfect agreement. Therefore, the conclusion on the formation of crystalline CoSi$_2$ phase in Co/Si MLF can be confidently made on the basis of only optical data. The HAXRD spectrum of the Co/Si MLF annealed at 1073 K is also changed drastically showing the formation of crystalline CoSi$_2$ phase.

SUMMARY

1. The real structures of the Fe/Au and Co/Pt MLFs were elucidated on the basis of the comparison of their experimental and computer-simulated optical properties. It was shown that all the investigated Fe/Au and Co/Pt MLFs have alloyed interfacial regions between pure components of about 1−2 nm in thickness. These regions noticeably influence on the resulting MO properties of the MLF.

2. The off-diagonal components of the DF for the spin-polarized Au and Pt sublayers in the Fe/Au and Co/Pt MLF were determined for the first time.

3. A set of Fe/Si MLF exhibiting a strong AF coupling were prepared and their measured MO and optical properties were compared with the simulated ones based on different models of MLF.

4. It was shown that neither Si, amorphous FeSi$_2$, ε-FeSi nor even metallic α-FeSi$_2$ could be considered as the interfacial spacers providing the strong AF coupling.

5. The optical properties of the spacer for the as-deposited Fe/Si MLF were extracted that strongly supports its metallic nature. This fact allows us to suggest that the AF coupling in the Fe/Si MLF is provided by the metallic spacer.

6. The calculated optical properties for the *B*2-phase FeSi silicide were compared with the experimentally extracted spectra of the silicide spacer that mediates a strong AF coupling in the Fe/Si MLF with relatively thick sublayers. The results also strongly suggest that the spacer is a metallic FeSi silicide.

7. Unlike the traditional structural methods, an optical approach

based on the comparison of the experimental and modelled as well as theoretically calculated optical properties allowed us to identify the structural transformations, induced in the investigated $3d$-TM/Si MLFs by IBM or thermal annealing, which were not detected by the traditional XRD method. We think that the differences in sensitivities is connected not with the difference in the probing depth but with basic conditions for the formation of x-ray diffracted beam and main features of the energy band structures.

ACKNOWLEDGMENTS

REFERENCES

1.   D. Weller, W. Reim, K. Spörl, and H. Brändle, *J. Magn. Magn. Mater.*, **93**: 183 (1991).
2.   W. B. Zeper, F. J. A. M. Greidanus, P. F. Carcia, and C. R. Fincher, *J. Appl. Phys.*, **65**: 4971 (1989).
3.   K. Sato, H. Ikekame, Y. Tosaka, K. Tsuzukiyama et al., *J. Magn. Magn. Mater.*, **126**: 572 (1993).
4.   Š. Višnovský, M. Nyvlt, V. Parizek, P. Kielar et al., *IEEE Trans. Magn.*, **MAG-29**: 3390 (1993).
5.   S. Uba, L. Uba, A. N. Yaresko, A. Ya. Perlov, V. N. Antonov, and R. Gontarz, *Phys. Rev. B*, **53**: 6526 (1996).
6.   E. R. Moog, J. Zak, and S. D. Bader, *J. Appl. Phys.*, **69**: 880 (1991).
7.   K. Takanashi, S. Mitani, M. Sano, H. Fujimori et al., *Appl. Phys. Lett.*, **67**: 1016 (1995).
8.   T. Katayama, H. Awano, and Y. Nishihara, *J. Phys. Soc. Jpn.*, **55**: 2539 (1986).
9.   Š. Višnovský, R. Lopusnik, M. Nyvlt, A. Das, R. Krishnan et al., *J. Magn. Magn. Mater.*, **198−199**: 480 (1999).
10.   K. Takanashi, S. Mitani, H. Fujimori et al., *J. Magn. Magn. Mater.*, **177−181**: 1199 (1998).
11.   K. Takanashi, S. Mitani, K. Himi, and H. Fujimori, *Appl. Phys. Lett.*, **72**: 737 (1998).
12.   K. Sato, E. Takeda, M. Akita, M. Yamaguchi, K. Takanashi et al., *J. App. Phys.*, **86**: 4985 (1999).
13.   L. Uba, S. Uba, V. N. Antonov, A. N. Yaresko et al., *Phys. Rev. B*, **62**: 13731 (2000).
14.   G Y. Guo and H. Ebert, *J. Magn. Magn. Mater.*, **156**: 173 (1996).
15.   T. Sato, Y. Tosaka, Horoshi Ikeme, M. Watanabe et al., *J. Magn. Magn. Mater.*, **148**: 206 (1995).
16.   W. Geerts, Y. Suzuki, T. Katayama, K. Tanaka, K. Ando, and S. Yoshida, *Phys. Rev. B*, **50**: 12581 (1994).

17.   E. E. Fullerton, J. E. Mattson, S. R. Lee et al., *J. Magn. Magn. Mater.*, **117**: L301 (1992); G. J. Strijkers, J. T. Kohlhepp, H. J. M. Swagten, and W. J. M. de Jonge, *Phys. Rev. B*, **60**: 9583 (1999).

18.   L. A. Clevenger, C. V. Thompson, R. C. Cammarata, and K. N. Tu, *Appl. Phys. Lett.*, **52**: 795 (1988).

19.   M. A. Hollander, B. J. Thijsse, and E. J. Mittemeijer, *Phys. Rev. B*, **42**: 5481 (1990).

20.   J. O. Olowolafe, M.-A. Nicolet, and J. W. Mayer, *Thin Solid Films*, **38**: 143 (1976).

21.   S. P. Murarka, *Silicides for VLSI Applications* (Orlando: Academic: 1983).

22.   C. J. Tsai and K. H. Yu, *Thin Solid Films*, **350**: 91 (1999).

23.   P. Knauth, A. Charaì, C. Bergman, and P. Gas, *J. Appl. Phys.*, **76**: 5195 (1994).

24.   B. Bokhonov and M. Korchagin, *J. Alloys Comp.*, **319**: 187 (2001).

26.   B. A. Julies, D. Knoesen, R. Pretorius, and D. Adams, *Thin Solid Films*, **347**: 201 (1999).

27.   D. Mangelinck, P. Gas, A. Grob, B. Pichaud, and O. Thomas, *J. Appl. Phys.*, **79**: 4078 (1996).

27.   J. Liu, J. Feng, B. Li, and J. Zhu, *J. Cryst. Growth*, **209**: 795 (2000).

28.   M. F. Wu, J. D. Wachter, A.-M. Van Bavel, R. Moons, A.Vantomme, H. Pattyn, G. Langouche, H. Bender, J. Vanhellemont, K. Temst, and Y. Bryunseraede, *J. Appl. Phys.*, **78**: 1707 (1995).

29.   Z. Rao, J. S. Williams, A. P. Pogany, D. K. Sood, and G. A. Collins, *J. Appl. Phys.*, **77**: 3782 (1995).

30.   S. B. Ogale, R. Joshee, V. P. Godbole, S. M. Kanetkar, and V. G. Bride, *J. Appl. Phys.*, **57**: 2915 (1985).

31.   D. L. Santos, J. P. de Souza, L. Amaral, and H. Boudinov, *Nucl. Instr. and Meth. B*, **103**; 56 (1995).

32.   J. Jagielski, M. Kopcewicz, A. Turos, and F. Eichhorn, *Nucl. Instr. and Meth. B*, **148**: 886 (1999).

33.   N. P. Barradas, C. Jeynes, K. P. Homewood et al., *Nucl. Instr. and Meth. B*, **139**: 235 (1998).

34.   M. Miloslavljevic, S. Dhar, P. Schaaf, N. Bibic et al., *Appl. Phys. A*, **71**: 43 (2000).

35.   E. E. Fullerton, J. E. Mattson, S. R. Lee et al., *J. Magn. Magn. Mater.*, **117**: L301 (1992).

36.   E. E. Fullerton, J. E. Mattson, S. R. Lee, C. H. Sowers et al., *J. Appl. Phys.*, **73**: 6335 (1993).

37.   A. Chaiken, R. P. Michel, and M. A. Wall, *Phys. Rev. B*, **53**: 5518 (1995).

38.   K. Inomata, K. Yusu, and Y. Saito, *Phys. Rev. Lett.*, **74**: 1863 (1995).

39.   E. E. Fullerton and S. D. Bader, *Phys. Rev. B*, **53**: 512 (1996).

40.   J. Kohlhepp, M. Valkier, A. van der Graaf, and F. J. A. Den Broeder, *Phys. Rev. B*, **55**: R696 (1997).

41.   G. J. Strijkers, J. T. Kohlhepp, H. J. M. Swagten, and W. J. M. de Jonge, *Phys. Rev. B*, **60**: 9583 (1999).

42.   J. A. Carlisle, A. Chaiken, R. P. Michel et al., *Phys. Rev. B*, **53**: R8824 (1996).

43.   J. J. de Vries, J. Kohlhepp, F. J. A. den Broeder, R. Coehoorn et al., *Phys. Rev. Lett.*, **78**: 3023 (1997).

44. R. Pretorius, C. C. Theron, A. C. Vantomme, and J. W. Mayer, *Critical Reviews in Solid State and Material Sciences*, **24**: 1 (1999).
45. J. R. Beattie and G. M. Conn, *Phil. Mag.*, **46**: 235 (1955).
46. R. M. A. Azzam and N. M. Bashara, *Ellipsometry and Polarized Light* (Amsterdam: North-Holland: 1977).
47. G. S. Krinchik, *Physics of Magnetic Phenomena* (Moscow: MGU Publisher: 1976) (in Russian).
48. P. G. Pells and M. Shiga, *J. Phys. C*, **2**: 1835 (1969).
49. V. N. Antonov, A. I. Baglyuk, A. Ya. Perlov et al., *Low Temp. Phys.*, **19**: 689 (1993).
50. J. H. Weaver, E. Colavite, D. W. Lynch, and R. Rosei, *Phys. Rev. B*, **19**: 3850 (1979).
51. J. H. Sexton, D. W. Lynch, R. I. Benbow, and N. V. Smith, *Phys. Rev. B*, **37**: 2879 (1988).
52. J. T. Wang, Z. Q. Li, and Y. Kawazoe, *J. Magn. Magn. Mater.*, **183**: 42 (1998).
53. Y. P. Lee, R. Gontarz, and Y. V. Kudryavtsev, *Phys. Rev. B*, **63**: 144402 (2001).
54. U. von Barth and L. Hedin, *J. Phys. C: Solid State Phys.*, **5**: 1629 (1972).
55. O. Jepsen and O. K. Andersen, *Solid State Commun.*, **9**: 1763 (1971).
56. J. Y. Rhee, B. N. Harmon, and D. W. Lynch, *Phys. Rev. B*, **55**: 4124 (1997).
57. J. M. Fallon, C. A. Faunce, H. J. Blythe, and P. J. Grundy, *J. Magn. Magn. Mater.*, **198−199**: 728 (1999).
58. V. S. Babu, A. S. Pavlovic, and M. S. Seehra, *J. Appl. Phys.*, **79**: 5230 (1996).
59. M. Amiotti, A. Borghesi, G. Guizetti, and F. Nava, *Phys. Rev. B*, **42**: 8939 (1990).
60. L. A. Clevenger and C. V. Thompson, *J. Appl. Phys.*, **67**: 1325 (1990).
61. Y. M. Gu and L. Fritsche, *J. Phys.: Condens. Matter*, **4**: 1905 (1992).
62. J. Y. Rhee, K. W. Kim, Yu. V. Kudryavtsev, and Y. P. Lee, *J. Korean Phys. Soc.*, **35**: S578 (1999).